ARTICLE

Check for updates

Ligand engineering to achieve enhanced ratiometric oxygen sensing in a silver cluster-based metal-organic framework

Xi-Yan Dong [1,2,4], Yubing Si [1,4], Jin-Sen Yang [1], Chong Zhang [1], Zhen Han [1], Peng Luo [1], Zhao-Yang Wang [1], Shuang-Quan Zang [1✉] & Thomas C. W. Mak [1,3]

Ratiometric luminescent oxygen sensing based on dual fluorescence and phosphorescence emission in a single matrix is highly desirable, yet the designed synthesis remains challenging. Silver-chalcogenolate-cluster-based metal-organic frameworks that combine the advantages of silver clusters and metal-organic frameworks have displayed unique luminescent properties. Herein, we rationally introduce $-NH_2$ groups on the linkers of a silver-chalcogenolate-cluster-based metal-organic framework (Ag_{12}bpy-NH_2) to tune the intersystem crossing, achieving a dual fluorescence-phosphorescence emission from the same linker chromophore. The blue fluorescence component has a 100-nm gap in wavelength and 8,500,000-fold difference in lifetime relative to a yellow phosphorescence component. Ag_{12}bpy-NH_2 quantifies oxygen during hypoxia with the limit of detection of as low as 0.1 ppm and 0.3 s response time, which is visualized by the naked eye. Our work shows that metal cluster-based MOFs have great potential in luminescent sensing, and the longer-lived charge-separated states could find more photofunctional applications in solar energy transformation and photocatalysis.

[1] Green Catalysis Center, and College of Chemistry, Zhengzhou University, 450001 Zhengzhou, China. [2] College of Chemistry and Chemical Engineering, Henan Polytechnic University, 454003 Jiaozuo, China. [3] Department of Chemistry, The Chinese University of Hong Kong, Shatin, New Territories, Hong Kong SAR, China. [4] These authors contributed equally: Xi-Yan Dong, Yubing Si. ✉email: zangsqzg@zzu.edu.cn

Oxygen quantification during hypoxia is essential in many fields of science and technology[1–3], and luminescent O_2 sensing has unique advantages, including full reversibility and a good precision and accuracy[2,3]. Commonly, the phosphorescence (Ph) emission intensity and lifetime are easily quenched to a certain extent by triplet oxygen, which becomes the basis of luminescent sensors used to detect molecular oxygen (Fig. 1a)[2–7]. However, it remains challenging to obtain an ultra-high sensitivity with minimum system error and to detect trace amounts of O_2. Scientists are pursuing self-calibrating ratiometric fluorescence (Fl)-phosphorescence (Ph) dual emission in a single luminescent matrix[8–12] with a longer-lived Ph component[13] (Fig. 1b), which can not only avoid the errors that are induced by the stoichiometric imbalance of the different emitting centers but also exhibit easily perceived color changes for rapid visual sensing (Fig. 1b). However, thus far, designing such integrated lumino-phores has achieved limited success for the following reasons: first, achieving balanced Fl and Ph intensities originating from the same luminophore is challenging for a ratiometric O_2 sensor because, as stated by Kasha's rule, photon emissions occur from only the lowest excited state[14]; second, phosphors that have both long-lived Ph (over milliseconds) and a high quantum yield (QY) at room temperature are difficult to prepare due to the intrinsic competition between the Ph lifetime and efficiency[15]; third, this type of luminophore must have a high oxygen permeability for free gas diffusion[2–8].

Metal-organic frameworks (MOFs) feature flexible secondary-building units (SBUs) and infinite tunable organic linkers, as well as abundant and distinctive pores or channels, and hence have shown great potential for separation and sensing[8–11,16–32]. Tra-ditionally, dual emission in MOFs is mostly achieved with lanthanide ion or luminescent linker on a host MOF framework as one emissive center and a post-introduced luminescent species including lanthanide ion, dye or carbon dot as another emissive center, which make it difficult to realize ultra-sensitive and ratiometric detection towards oxygen gas[11]. Silver-

chalcogenolate-cluster-based metal-organic frameworks (SCC-MOFs)[33–38], in which each SBU consists of tens of silver and chalcogen atoms, have become a new member of the MOF family. SCC-MOFs combine the advantages of silver clusters[39–43] and MOFs[8–11,16–32]; SCC-MOFs have shown remarkably improved luminescent properties relative to discrete silver clusters and unique excellent luminescent responses for sensing gases and volatile organic compounds (VOCs)[33–37]. We previously reported a SCC-MOF, that is, $Ag_{12}bpy$[33], ($[Ag_{12}(S^tBu)_8(CF_3COO)_4(b-py)_4]_n$, bpy = 4,4'-bipyridine), whose single green Ph is sensitive to oxygen (Fig. 1c). We hypothesize that, according to the interligand trans-metallic charge-transfer (ITCT) emission mechanism of $Ag_{12}bpy$[33,36], the additional introduction of the organic ligand-centered Fl emission can achieve dual Fl-Ph emission centers in the host framework of a SCC-MOF, whose Ph component is supposed to be sensitive to oxygen; the functional modification of the MOF linker can modulate the Ph properties by changing the intersystem crossing (ISC) efficiency; thus, ratiometric oxygen sensing could be achieved in a SCC-MOF with a higher sensitivity.

Here, we first modified the bpy linkers using amino groups bearing lone-pair electrons, i.e., a blue emitting 3-amino-4,4'-bipyridine (bpy-NH_2)[31,36] moiety, and changed the synthesis method (Supplementary Fig. 1), yielding a new isostructural complex, $[Ag_{12}(SBu^t)_8(CF_3COO)_4(bpy-NH_2)_4]_n$ ($Ag_{12}bpy-NH_2$) (Fig. 1c). The incorporation of amino groups has two significant functions: first, a blue sub-nanosecond Fl component (0.37 ns under vacuum) centered at ~456 nm (Figs. 1c and 2), in addition to a yellow Ph component at 556 nm, has been achieved; second, incorporating amino groups strongly triggers spin-orbit coupling (SOC) and increases the rate of ISC to boost triplet excitons, thus prolonging the lifetime of the Ph component by ~15,000-fold, from submicroseconds (0.2 μs) to milliseconds (3.12 ms), which occurs concomitantly with an increase in the QY from 12.1 to 14.6% under vacuum. Thus, the large gap of ~100 nm between the emission wavelengths and the increased lifetime difference
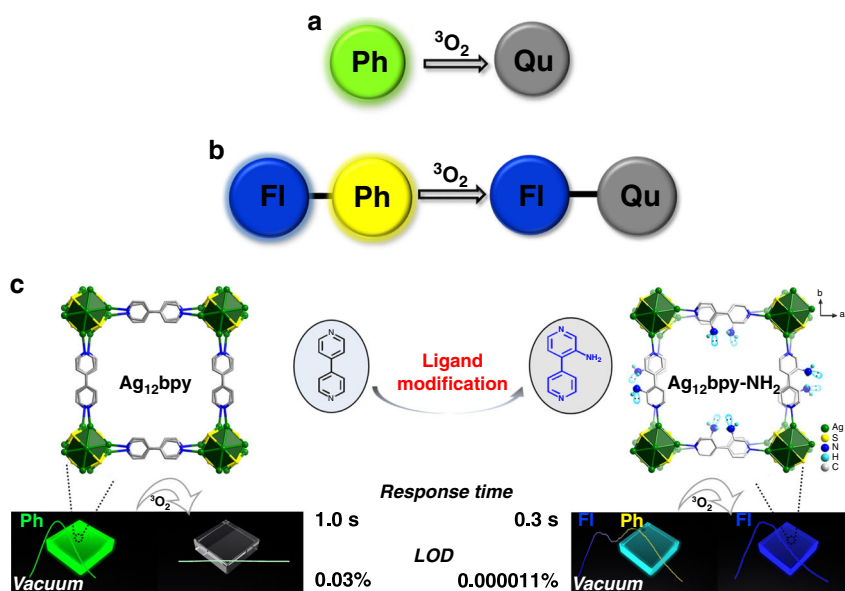

Fig. 1 Schematic luminescent oxygen sensing and ligand modification of SCC-MOFs. Schematic of oxygen quenching sensing based on **a** a single Ph emission and **b** dual Fl-Ph emissions. Fl = Fluorescence, Ph = Phosphorescence, Qu = Quenched. Each colored circle represents an emissive center. **c** Schematic of $Ag_{12}bpy$ crystals emitting a single green color under vacuum that is quenched by oxygen with a response time of approximately 1.0 s and an LOD of 0.03%; the isostructural $Ag_{12}bpy-NH_2$ crystal modified with $-NH_2$ groups on the bpy linkers emits nearly a different cyan color that is composed of a blue Fl and a yellow Ph component under a certain vacuum, but only emits blue Fl under oxygen conditions. Note: the color emitted by $Ag_{12}bpy-NH_2$ is variable under different vacuum conditions (see the main text). When using $Ag_{12}bpy-NH_2$ as a ratiometric oxygen sensor, the response time decreased to 0.3 s and the LOD dropped to 0.000011%.
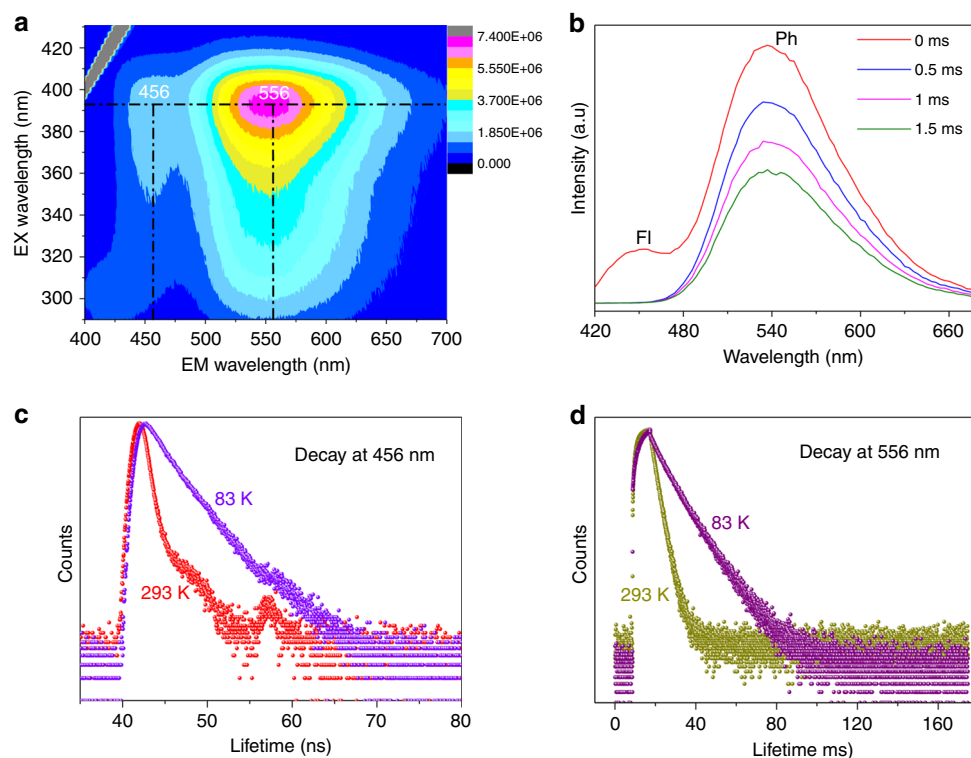
Fig. 2 Photoluminescence properties of Ag$_{12}$bpy-NH$_2$. a The three-dimensional excitation-emission matrix (3D-EEM) spectra of Ag$_{12}$bpy-NH$_2$ under a vacuum at room temperature. The two emission centers are located at ~456 and 556 nm. **b** Prompt (0 ms) and time-delayed (0.5, 1, 1.5 ms) emission of solid-state Ag$_{12}$bpy-NH$_2$ at room temperature under a vacuum. **c** Time-resolved Fl (456 nm) and **d** Ph (556 nm) decay traces of Ag$_{12}$bpy-NH$_2$ under a vacuum at 293 and 83 K.

(~8.5 × 10^6 times) of the Ph and Fl bands, combined with the highly oxygen-permeable framework structure, enable Ag$_{12}$bpy-NH$_2$ to function as a single-component Fl-Ph ratiometric sensor for molecular oxygen in which ultrafast responses towards trace oxygen gas are achieved in 0.3 s, and the limit of detection (LOD) is as low as 0.1 ppm; this response can be visualized by variations in the color, which is dependent on the O$_2$ concentration below 20 ppm. To the best of our knowledge, Ag$_{12}$bpy-NH$_2$ is the first report of a Fl-Ph dual-emissive MOF that has a record-breaking LOD and response speed[8–10,19–25]. By the further introduction of bulk −CH$_3$ groups on the partial bpy linkers, which interferes with the oxygen collision dynamics, we then prepared another isostructural mixed-linker Ag$_{12}$bpy-NH$_2$/CH$_3$, which extended the ratiometric sensing range. Such long-lived metal-cluster ensembles are promising materials for sensing, photocatalysis, sensitization of electrochemical solar cells, and solar-energy-harvesting applications.

Results

Structure and photoluminescence of Ag$_{12}$bpy-NH$_2$. Compared to bpy, bpy-NH$_2$ has an unchanged length and unaltered connectivity (Fig. 1c); however, introducing an amino group at the 3-position of bpy greatly alters the reaction conditions: the synthesis method used for the Ag$_{12}$bpy structures that are synthesized in mixed CH$_3$CN and C$_2$H$_5$OH is no longer applicable for Ag$_{12}$bpy-NH$_2$. After sustained attempts, isomorphous single crystals of Ag$_{12}$bpy-NH$_2$ were prepared by the reaction of AgS^{t}Bu, CF$_3$COOAg and bpy-NH$_2$ in a mixed solvent of NH$_4$OH and CH$_2$Cl$_2$ (Supplementary Fig. 1), suggesting that the used solvents play key roles in the structure of SCC-MOFs. The single-crystal X-ray diffraction (SCXRD) analysis revealed that Ag$_{12}$bpy-NH$_2$ and Ag$_{12}$bpy belong to the same tetragonal space group (No. 121) and have identical silver cluster subunits, and every (−S^{t}Bu,

−OOCCF$_3$) ligand and N-containing linker have identical ligand coordination modes (Fig. 1c and Supplementary Figs. 2 and 3). The phase purity and chemical formula of Ag$_{12}$bpy-NH$_2$ were further verified by elemental analysis, powder X-ray diffraction (PXRD) and thermogravimetric analysis (TGA) (Supplementary Figs. 4 and 5). The amino groups anchored on the linker slightly decrease the pore void space from 21.6% for Ag$_{12}$bpy to 17.5% for Ag$_{12}$bpy-NH$_2$, as calculated from the X-ray structural data obtained by PLATON (see Methods) and verified by the measurement of the 77 K N$_2$ sorption isotherm (Supplementary Fig. 6). Compared to that of Ag$_{12}$bpy, the UV-vis absorption intensity of Ag$_{12}$bpy-NH$_2$ obviously increased before 600 nm and redshifted, extending to 680 nm (Supplementary Fig. 7). The enhancement before 450 nm suggests that new (n, π*) transitions possibly occurred because of the introduction of the −NH$_2$ group with a lone-pair on the pyridine ring (Fig. 1c, Supplementary Figs. 8 and 9).

The crystals of Ag$_{12}$bpy-NH$_2$ exhibit a blue emission in air and in solution not degassed by N$_2$, which is similar to the blue Fl color of the pure bpy-NH$_2$ linker[36] in the solid state with a lifetime of approximately 3.59 ns (Table 1 and Supplementary Figs. 10–12). In contrast, amino-free Ag$_{12}$bpy exhibits color-variable Ph in various organic solvents[33]. These observations implied that the Ph component of Ag$_{12}$bpy-NH$_2$ is likely to be much more sensitive to oxygen in solution than Ag$_{12}$bpy. To validate this hypothesis, we subsequently measured the luminescence properties of Ag$_{12}$bpy-NH$_2$ under a high vacuum at room temperature, which resulted in highly separated dual emissions (Fig. 2a, b and Table 1) upon excitation with a 370 nm UV light. One emission is the ligand-based fluorescence emission centered at ~456 nm, which has a lifetime of 0.37 ns at room temperature and 2.48 ns at 83 K (Fig. 2c); this emission lifetime of 0.37 ns is only one-tenth the lifetime of the solid-state bpy-NH$_2$ ligand (3.59 ns, Table 1 and

Table 1 Luminescent properties of the compounds.

Compound	Fluorescence			Phosphorescence		
	λ_{max} (nm)	τ_f (ns)	QY(%)	λ_{max} (nm)	τ_p (ms)	QY(%)
bpy-NH$_2$	420	3.59	30.56	No	No	No
Ag$_{12}$bpy	No	No	No	507	2×10^{-4}	12.10
Ag$_{12}$bpy-NH$_2$	456	0.37	2.54	556	3.12	14.62
Ag$_{12}$bpy-CH$_3$	No	No	No	500	6.8×10^{-5}	3.06
Ag$_{12}$bpy-F	No	No	No	530	3.5×10^{-4}	21.80

λ_{max} (nm) the maximum of emission wavelength, τ_f the lifetime of fluorescence component, τ_p the lifetime of phosphorescence component, QY quantum yield. Unless otherwise stated, at 20 °C under vacuum.

Supplementary Fig. 11); the Fl QY is significantly reduced from 30.56 to 2.54%, and the Fl peak is also redshifted to 456 nm compared to the Fl peak of solid-state bpy-NH$_2$ (420 nm) due to metal coordination (Supplementary Fig. 10). Another emission is an outstanding yellow Ph emission located at 556 nm, with emission lifetimes of 3.12 ms at 293 K and 10.55 ms at 83 K (Fig. 2d), which is an increase of 15,000 times compared to the room-temperature Ph lifetime of 200 ns observed for unsubstituted Ag$_{12}$bpy; in addition, the quantum efficiency increased to 14.62% compared to the 12.10% quantum efficiency obtained for unsubstituted Ag$_{12}$bpy under vacuum (Table 1). Most importantly, the separation of the Ph peak at 556 nm from its Fl peak at 456 nm is truly enhanced, and the Ph intensity greatly surpasses the Fl intensity under vacuum (Fig. 2b). The significant decrease in the ligand-based Fl lifetimes of Ag$_{12}$bpy-NH$_2$ from 3.59 to 0.37 ns, which is accompanied by a considerable increase in the Ph lifetime from 0.2 μs to 3.12 ms (Table 1), suggested the occurrence of an efficient ISC process from the lowest singlet to the lowest triplet excited states (vide infra). The 15,000-fold enhancement in the Ph lifetime is an unprecedented phenomenon among luminescent MOFs[19–28,33–38] and metal clusters[39–43], even in metal-containing phosphors[12,13,44–46], which means that the triplet excited state(s) of Ag$_{12}$bpy-NH$_2$ is capable of responding to oxygen molecules with a sensitivity of one-15,000th of the original sensitivity of unsubstituted Ag$_{12}$bpy if one merely considers the lifetime factor. Of course, this also presents a challenge for obtaining precise measurements in the range of hypoxia.

Ratiometric optical oxygen sensing. By balancing the Fl and Ph intensities upon excitation at a single wavelength in which the Ph component has a considerably long decay time (3.12 ms) and highly separated dual emissions, as well as highly oxygen-permeable channels (Figs. 1, 2 and Table 1), Ag$_{12}$bpy-NH$_2$ provides a platform to serve as a ratiometric O$_2$ sensor and is ideal for the characterization of nearly anoxic systems. Because of the ultrasensitive oxygen quenching effect of Ag$_{12}$bpy-NH$_2$, measurements must be carried out in a high vacuum system because an inert atmosphere (less than 10 ppb of oxygen) is very difficult to achieve for standard O$_2$ gas sensing. To overcome the difficulty of the measurement, we used a homemade measurement system in conjunction with a gas absorption analyzer (BEL-max physisorption analyzer) to ensure the control of the ultrahigh vacuum with high precision and a spectrofluorometer (HORIBA FluoroLog-3) that was connected to a gas absorption analyzer (MicrotracBEL Belsorp Max) by an optical fiber. An image of this set up for O$_2$ sensing under an ultrahigh vacuum is shown in Supplementary Fig. 13 with a detailed explanation.

Ratiometric optical oxygen sensing using dual-emitting Ag$_{12}$bpy-NH$_2$ was achieved by monitoring the response at different oxygen partial pressures (Fig. 3a, b). Oxygen-insensitive blue Fl served as the 'reference' signal, and oxygen-

quenchable Ph served as the response signal for readout. The ratio of the nearly invariant fluorescence response (λ_{Fl} = 456 nm) to the oxygen-dependent Ph response (λ_{Ph} = 556 nm) steadily increased with increasing oxygen levels. Overall, 99.9% of the phosphorescence response was quenched at a pressure of 44.3 Pa. In the range from vacuum (10^{-3} Pa) to 2.4 Pa, a linear Stern-Volmer plot (SVP)[2,8,33] was observed (R^2 = 0.993) (Fig. 3c), and a continuous linear color change from blue to yellow was observed in the CIE coordinate diagram, facilitating the identification of the O$_2$ pressure by the naked eye (Fig. 3d). The calculated Stern-Volmer constant[2,8,33] (K_{sv}) was 2.25 kPa^{-1}, and the LOD at 1% quenching was 11.4 mPa. Beyond this point, the Fl/Ph plot continued to increase up to 44.3 Pa, which was nearly equal to ambient levels (that is, 21% O$_2$) (Fig. 3b). Compared to the LOD (32 Pa) of Ag$_{12}$bpy, the LOD of Ag$_{12}$bpy-NH$_2$ was low (11.4 mPa), only 3.56×10^{-6}% of the original value. To further explore the oxygen sensitivity, quick response and recyclability of this system, we recorded the transient luminescence response curves of the dual-emission peak intensity under alternating air/vacuum conditions at RT (Fig. 3e); the nearly invariant Fl intensity at 456 nm (blue straight line) and the on-off Ph intensity with sharp contrast at 556 nm (black folding line) demonstrated that Fl is a good reference signal. The air-quenching response time was 0.3 s (Fig. 3f), which is as fast 3.3 times as that of Ag$_{12}$bpy (~1 s)[33], and is concomitant with the synchronous visual color change (Fig. 3d). Compared to the Ph lifetime of Ag$_{12}$bpy (0.2 μs)[33], we think that the elongated Ph lifetime of Ag$_{12}$bpy-NH$_2$ of 3.12 ms mainly contributes to the enhanced sensitivity. The calculated void space of Ag$_{12}$bpy-NH$_2$ was 17.5%, which is slightly lower than that of Ag$_{12}$bpy (21.6%), as demonstrated by the 77 K N$_2$ absorption isotherm (Supplementary Fig. 6). Ag$_{12}$bpy-NH$_2$, with an LOD as low as 0.11 ppm, is applicable for nearly anoxic systems with oxygen levels in the range of 0.1–24 ppm and has sensitivities that are orders of magnitude above those of conventional sensing MOFs[19–28,33–38]. Ag$_{12}$bpy-NH$_2$ opens the door to completely new applications for monitoring oxygen in previously inaccessible concentration regions and is likely to become invaluable in diverse fields of science and technology.

Extending the sensing range of O$_2$ by introducing bulky −CH$_3$ groups. Considering the dynamic O$_2$-quenching mechanisms of these SCC-MOF$_S$, one can imagine that other factors that affect the oxygen collision process would also tune the sensitivity. Based on this hypothesis, we prepared another isostructural SCC-MOF, Ag$_{12}$bpy-CH$_3$ (Fig. 4a, b), where the large methyl group, which contributes minimally to the excited state, is expected to intervene in the collision process (Supplementary Figs. 14–19). In contrast to Ag$_{12}$bpy-NH$_2$, an opening effect and desorption lag are observed in the absorption isotherms of Ag$_{12}$bpy-CH$_3$ at 77 K (Fig. 4c), and a decrease in the pore volume also appeared due to the relatively increased size of the −CH$_3$ groups, suggesting that the possible weakly viscous interactions between the host and
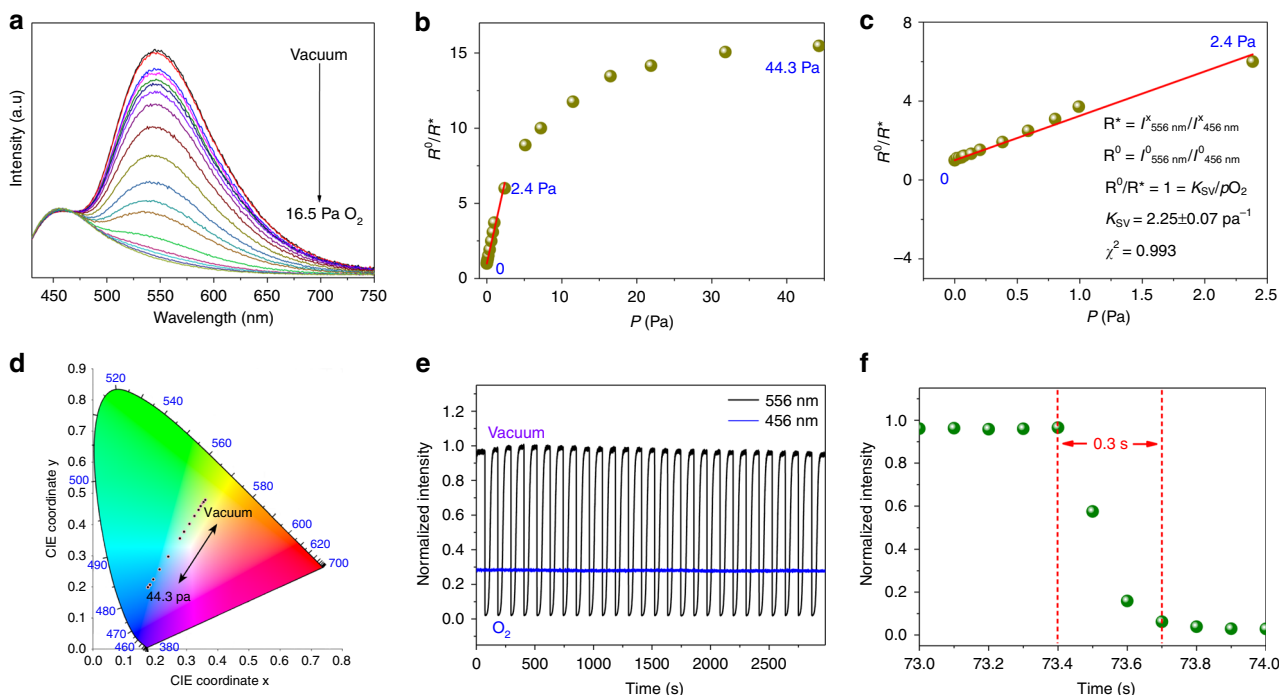
Fig. 3 Luminescent oxygen sensing. a Emission spectra of $Ag_{12}bpy$-NH_2 under different oxygen pressures from 0 to 16.5 Pa (excited at 365 nm). **b** The correlation between the ratiometric photoluminescence response and O_2 partial pressure in the range of 0–44.3 Pa. **c** Representative Stern-Volmer plot of O_2 in the range of 0–2.4 Pa. **d** The emission color-changing range for ratiometric oxygen sensing. **e** Reversible luminescence cycles of $Ag_{12}bpy$-NH_2 under alternating exposure to air/vacuum: on-off Ph (black folding line) and invariant Fl (blue straight line). **f** Enlargement of the response transient curves of $Ag_{12}bpy$-NH_2 exposed to air. The response time of the air-quenching Ph component is ~0.3 s (the response time is defined as the time corresponding to a 90% decrease in the emission intensity when the gas phase is changed from vacuum to air).

guest hindered gas from freely going in and out. $Ag_{12}bpy$-CH_3 merely emits a single green luminescence response (Fig. 4d, Table 1) under vacuum and weakly luminesces in air, implying that the Ph emission of $Ag_{12}bpy$-CH_3 is much less sensitive to oxygen than that of $Ag_{12}bpy$-NH_2. The oxygen-sensing experiments showed that $Ag_{12}bpy$-CH_3 can work in the range of higher oxygen concentrations (0.1–21% in air, Fig. 4d). To further understand the origin of the insensitivity induced by the −CH_3 groups, we prepared a molecular oxygen inclusion compound, namely, $Ag_{12}bpy$-CH_3·O_2, at 80 K (Fig. 4b); the channels of $Ag_{12}bpy$-CH_3·O_2 contained the most preferred position of O_2 molecules, which had a site occupancy of 0.1 and were the nearby −CH_3 groups, and the separation between the O_2 and −CH_3 groups (O···H = 2.29 Å, O···C = 2.65 Å) was much smaller than that between the O_2 and bpy moieties (4.05 Å) (Supplementary Fig. 20). Considering that the kinetic diameter of O_2 is 3.46 Å[32] and that the −CH_3 groups are minimally involved in the excited states, we proposed that O_2 molecules have fewer chances to dynamically collide with LUMO localized bpy-CH_3 in $Ag_{12}bpy$-CH_3 and can not effectively switch off their emission, resulting in insensitivity. Then, further than that, a mixed-linker crystal of $Ag_{12}bpy$-NH_2/CH_3 (with a bpy-NH_2:bpy-CH_3 ratio of 1:100, as determined by ^{1}H NMR, Supplementary Figs. 21 and 22) was prepared and functions in the O_2 concentration range of 20 ppm to 0.1% (Fig. 4e). The contrasting effect of the −NH_2 and −CH_3 groups on the oxygen-sensing performance indicate that the proposed dynamic quenching process by oxygen is a photophysical process, during which the interactions between molecular (triplet) oxygen and the excited electronic states of the SCC-MOFs are controlled by the emissive lifetime and the permeability or diffusion rate of oxygen. The −NH_2 groups, markedly enhanced the sensitivity by generating an oxygen-insensitive reference blue Fl signal and simultaneously elongating the yellow

Ph component lifetime; while, the −CH_3 groups mainly decrease the sensitivity by erecting barriers of O_2 diffusion in the channels of the SCC-MOFs. The balance modulation can tune the sensing range of oxygen. Therefore, engineering the ligands on SCC-MOFs is deemed to be a powerful method of modulating the remarkable luminescent sensing functionality.

Luminescent properties of isostructural SCC-MOFs with different substituents. To gain further insights into the origin of the dual emission and the long-lived Ph lifetime of $Ag_{12}bpy$-NH_2, we compared two additional isostructural crystals, $Ag_{12}bpy$-CH_3 containing bpy-CH_3 linkers with an electron-donating methyl group and $Ag_{12}bpy$-F[36] containing 3-fluorine-4,4′-bipyridine (bpy-F) bearing an electron-withdrawing fluoro group (Table 1). Based on the above mentioned experimental results, we have observed that in the absence of an efficient Fl emission produced by bpy-CH_3 and bpy-F, only a single phosphorescence response appears in $Ag_{12}bpy$-CH_3 and $Ag_{12}bpy$-F. Similar to most metal-containing phosphors involving a π^*-orbital-involved charge-transfer emission[12,44,45], electron-donating −CH_3 groups likely destabilize the π^* orbital, decrease the lifetime to approximately 68 ns under vacuum, and cause a blueshift of only 7 nm under vacuum; however, electron-withdrawing −F groups have the opposite effect and increase the lifetimes (351 ns[36], Table 1) and result in a redshift of more than 20 nm. This variation induced by the electron-donating/withdrawing effect still occurred on the same order of magnitude of submicroseconds, indicating that the inherent emissive excited state did not change. In stark contrast, the Ph component of $Ag_{12}bpy$-NH_2 unprecedentedly increased drastically by over four orders of magnitude. We proposed that the −NH_2 substituent might take part in the emissive triplet state and promote ISC from the singlet to triplet state. The Fl
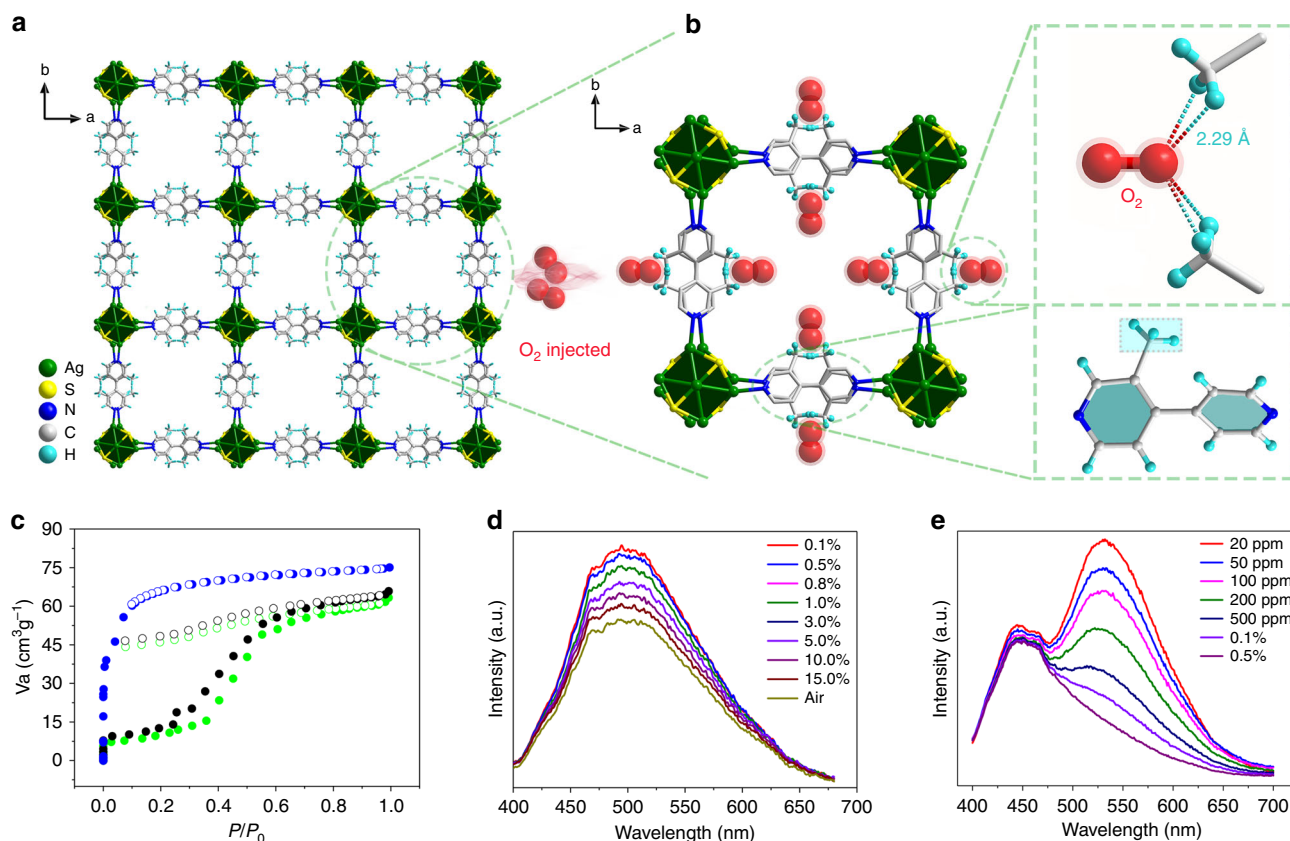
Fig. 4 The oxygen molecule position in Ag$_{12}$bpy-CH$_3$ and the oxygen-sensing performance. a Channels of Ag$_{12}$bpy-CH$_3$ and **b** O$_2$-inclusion of Ag$_{12}$bpy-CH$_3$·O$_2$, as viewed along the c-axis. The most preferable positions of the oxygen molecules are displayed. The smallest separation between O$_2$ and the −CH$_3$ groups (O···H) is equal to 2.29 Å. Color code: Ag, green; S, yellow; C, gray; N, blue; H, light turquoise; O, red. The H atoms of bpy and −^{t}Bu groups of the host backbone are omitted for clarity. **c** N$_2$ adsorption/desorption isotherms of Ag$_{12}$bpy-NH$_2$ (blue line), Ag$_{12}$bpy-CH$_3$ (green line) and Ag$_{12}$bpy-NH$_2$/CH$_3$ (1:100) (black line) at 77 K. **d** Oxygen-dependent emission intensity of Ag$_{12}$bpy-CH$_3$ in the range of 0.1% to ambient air conditions. **e** Oxygen-dependent dual-emission intensity of Ag$_{12}$bpy-NH$_2$/CH$_3$ (1:100) in the range of 20 ppm to 0.5%.

component of Ag$_{12}$bpy-NH$_2$, with a lifetime of 0.37 ns, possibly originates from the mixed ^{1}(n, π*) and ^{1}(π, π*) excited singlet states; the Ph component of Ag$_{12}$bpy-NH$_2$ with a lifetime of 3.12 ms, might originate from the mixed ^{3}ITCT and ^{3}(n, π*) triplet states in which the participation of ^{3}(n, π*) could facilitate ISC and probably varies the characteristics of the lowest emissive triplet states, eventually leading to a 15,000-fold elongation of the lifetime and a more than 40-nm redshift. The incomplete electron communication between the two emissive states could result in a Fl-Ph dual emission (Supplementary Fig. 23).

The amino groups modulating the emissive triplet states and prompting ISC. The Fl energy of the free bpy-NH$_2$ ligand is dependent on the solvent (Supplementary Fig. 10), which is consistent with the charge-transfer (CT) characteristics and further indicates that the emissive singlet state could combine the ^{1}(n, π*) state with the ^{1}(π, π*) state. In contrast, the Fl component of Ag$_{12}$bpy-NH$_2$ is independent of the solvent (Supplementary Fig. 12); it is likely that the ligand-based ^{1}(π, π*) state may be the localized excited state at bpy-NH$_2$ linkers of Ag$_{12}$bpy-NH$_2$ (Supplementary Fig. 23). From these comparison data, a schematic of the evolving luminescence is presented: the blue Fl component of the ligand, which stems from the emissive singlet state, was considerably decreased by 92.8%, which is calculated from the lifetime. For Ag$_{12}$bpy, we previously ascribed the Ph component to ITCT (S/Ag → bpy)[36]. Thus, the Ph component of Ag$_{12}$bpy-NH$_2$ from the *ITCT triplet state (S/Ag → bpy-NH$_2$) redshifted to 556 nm, and its intensity increased; the most

attractive feature of this system is the increase in the lifetime to the millisecond range. The trend between Fl and Ph indicates that (i) the emissive triplet state of Ag$_{12}$bpy-NH$_2$ has a lower energy and is relatively stable, and (ii) the charge transfer and energy transfer from the bpy-NH$_2$-based ^{1}(π, π*)-dominated emissive single state to the ^{3}ITCT (S/Ag → π* of bpy-NH$_2$) triplet state was mixed with a small amount of ^{3}(n, π*). Therefore, incorporating the −NH$_2$ group into the bpy linkers significantly changed molecular energy levels (see the calculated molecular orbitals and analysis of Ag$_{12}$bpy-NH$_2$ shown in Supplementary Figs. 23–26 and Supplementary Table 1).

Moreover, because the rate constant of the ISC from singlet to triplet excited states is proportional to the square of the SOC constant, we examined 20 of the lowest singlet-triplet transitions by performing calculations for Ag$_{12}$bpy-NH$_2$, Ag$_{12}$bpy-CH$_3$, Ag$_{12}$bpy-F, and Ag$_{12}$bpy (Fig. 5). Considering that spin-flipping may be enhanced by the resonance variation with an increased n-value orbital participation[47], the triplet excited states with a small vertical excitation energy gap (ΔE$_{S1Tn}$ less than 0.15 eV) were included. Ag$_{12}$bpy-NH$_2$ has far more triplet excited states (T$_n$) close to S$_1$ in energy, and the smaller energy gap and higher SOC would well support the efficient ISC process to generate more triplet states with much longer lifetimes. For Ag$_{12}$bpy-NH$_2$, the transitions between S$_1$ and T$_n$ are the transitions from locally excited (LE) states ^{1}(π, π*) to charge-transfer triplet states mixed with ^{3}(n, π*) and ^{3}ITCT, which would result in the high SOC according to the El-Sayed rules[48–50]. Thus, the participation of the −NH$_2$ units actually
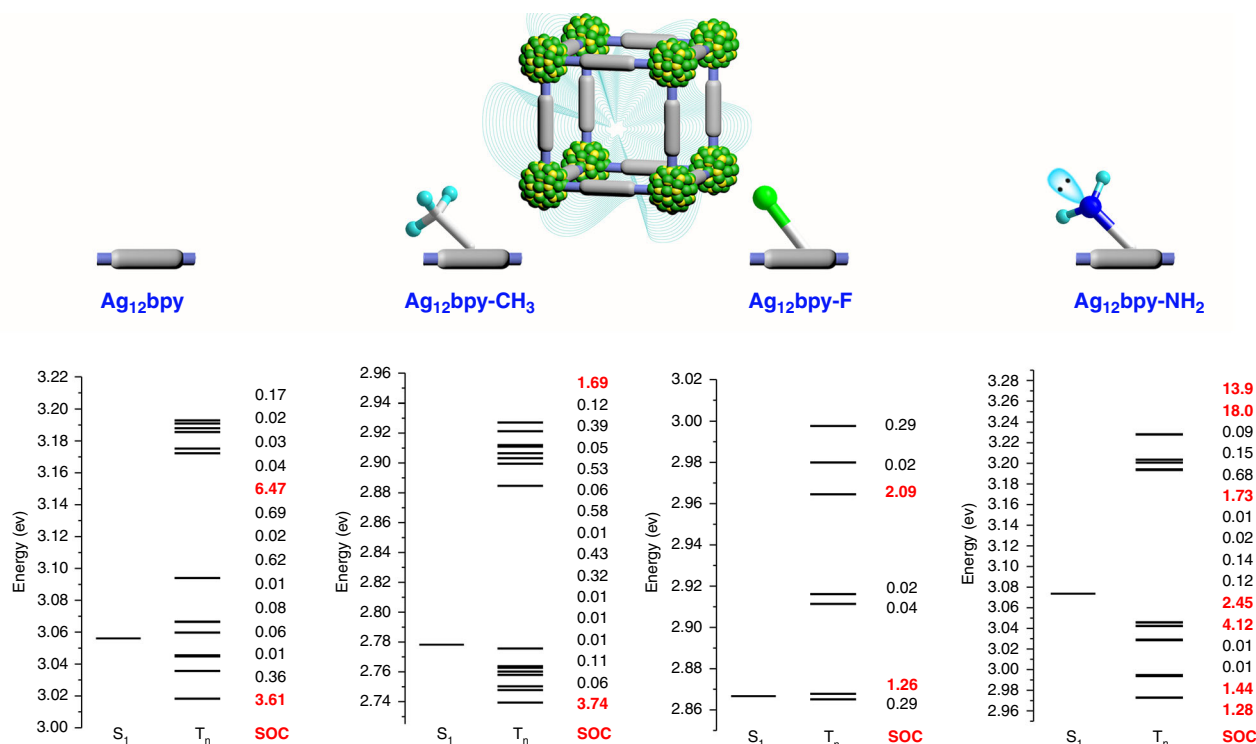
Fig. 5 Energy level diagram and SOC constants. The SOC values are in cm^{-1}, and the high values ($>1\ cm^{-1}$) are in bold red. There are 4, 8, 1, and 10 triplet states that are lower than the corresponding singlet state of the pristine, $-CH_3$, $-F$, and $-NH_2$ substituted molecules. Considering that the resonance structures may promote ISC[47], the higher triplet states with a low energy gap ($\Delta E_{S_1T_n} < 0.15\ eV$) were displayed.

results in a new facile pathway for the ISC process to occur between S_1 and T_n, increasing the effective ISC to achieve an efficient longer-lived Ph response.

Discussion

In summary, we have devised a simple yet powerful strategy to tune the delicate balance between the emissive intraligand singlet states and CT triplet states, which enables the observation of dual Fl and Ph peaks with a 100-nm separation and an 8,500,000-fold lifetime gap, and have provided the first model of dual Fl-Ph ultrasensitive ratiometric O_2 sensing in the range of hypoxia based on a single-component SCC-MOF. The introduced amine groups ($-NH_2$) with lone-pair electrons strengthened SOC and facilitated ISC and, henceforth, induced a 15,000-fold enhancement in the Ph lifetime from submicroseconds to milliseconds. Furthermore, using a substituent-mediated strategy ($-CH_3$ and mixed $-NH_2$ and $-CH_3$ groups) to interfere with the dynamic quenching process of O_2 extends the sensing concentration range. The bright long-lifetime excited states and the homogeneously ordered spatial separation of metal clusters enable these metal-cluster ensembles to be used in sensing, imaging, photocatalysis, and solar-energy-harvesting applications.

Methods

Reagents. All reagents and solvents used were of commercially available reagent grade and used without further purification. AgS^tBu was prepared from the reaction of molar equivalents of Ag_2O and HS^tBu in Et_3N.

Synthesis of bpy-NH$_2$ and bpy-CH$_3$. 3-amino-4,4′-bipyridine (bpy-NH$_2$) and 3-methyl-4,4′-bipyridine (bpy-CH$_3$) were prepared from Suzuki coupling of 3-amino-4-chloropyridine or 3-methyl-4-chloropyridine and pyridine-4-boronic acid[31].

Preparation of Ag$_{12}$bpy-NH$_2$ single crystals. 3-amino-4,4′-bipyridine (bpy-NH$_2$, 10 mg) and 10 μL ammonium hydroxide were added to a solution of AgS^tBu

(15 mg), CF_3COOAg (6 mg) and CH_2Cl_2 (4 mL) under stirring to obtain a clear solution under ambient conditions. The reaction solution was filtered, and the filtrate was slowly evaporated in air to give bulk colourless crystals, which were rinsed with CH_2Cl_2, filtered and dried in air to produce Ag$_{12}$bpy-NH$_2$ ($C_{80}H_{108}Ag_{12}F_{12}N_{12}O_8S_8$) in ~30% yield based on Ag. Elemental analysis (calculated): C 30.55, H 3.46, N 5.34, S, 8.16%; Found: C 30.42, H 3.53, N 5.41, S, 8.09%.

Preparation of Ag$_{12}$bpy-CH$_3$ single crystals. Single crystals of Ag$_{12}$bpy-CH$_3$ were prepared in a manner like the preparation of Ag$_{12}$bpy-NH$_2$, except bpy-NH$_2$ was replaced by bpy-CH$_3$; a yield of ~55% was achieved based on Ag. Ag$_{12}$bpy-CH$_3$ ($C_{84}H_{112}Ag_{12}F_{12}N_8O_8S_8$) Elemental analysis (calculated): C 32.12, H 3.59, N 3.57, S, 8.17%; Found: C 32.18, H 3.64, N 3.56, S, 8.11%.

Preparation of Ag$_{12}$bpy-CH$_3$·O$_2$ single crystals. A single crystal of Ag$_{12}$bpy-CH$_3$ was evacuated to a pressure of $10^{-3}-10^{-4}$ Pa. Next, pure pressurized O_2 was backfilled at 77 K through the open end of the capillary until the pressure reached 30 kPa. Subsequently, the open end was sealed in situ to maintain the crystal under high pure O_2 pressure surroundings, producing Ag$_{12}$bpy-CH$_3$·O$_2$, which was subjected to SCXRD analysis at 80 K.

Preparation of Ag$_{12}$bpy-NH$_2$/CH$_3$ crystals. Crystals of Ag$_{12}$bpy-NH$_2$/CH$_3$ were prepared similar to Ag$_{12}$bpy-NH$_2$, except the mixture of bpy-NH$_2$ and bpy-CH$_3$ were added into the reaction solution simultaneously. Different ratios of bpy-NH$_2$ to bpy-CH$_3$ were attempted according to the relative intensity of two emission peaks. The optimized ratio of bpy-NH$_2$:bpy-CH$_3$ = 1:100 was determined by ^{1}H NMR (Supplementary Fig. 22).

Crystallographic data collection and refinement of the structure. SCXRD measurements of Ag$_{12}$bpy-NH$_2$ and Ag$_{12}$bpy-CH$_3$ were performed at 150 K and measurements of Ag$_{12}$bpy-CH$_3$·O$_2$ were performed at 80 K on a Rigaku XtaLAB Pro diffractometers with Cu-Kα radiation ($\lambda = 1.54184$ Å). Data collection and reduction were performed using the program CrysAlisPro[51,52]. All the structures were solved with direct methods (SHELXS)[53] and refined by full-matrix least squares on F^2 using OLEX2[54], which utilizes the SHELXL-2015 module[55]. All atoms were refined anisotropically, and hydrogen atoms were placed in calculated positions with idealized geometries and assigned fixed isotropic displacement parameters. Detailed information about the X-ray crystal data, intensity collection procedure and refinement results for Ag$_{12}$bpy-NH$_2$, Ag$_{12}$bpy-CH$_3$, and Ag$_{12}$bpy-CH$_3$·O$_2$ is summarized in Supplementary Table 2.

Calculation of void space. The fraction of void space was calculated from the X-ray structural data of $Ag_{12}bpy-NH_2$ by PLATON/VOID: The unit cell was filled with the atoms from the structural model, and each specific atom was assigned its respective van der Waals radius. A grid search generated a list of grid points with a minimum distance of 1.2 Å from the nearest van der Waals surface. This list of grid points was then used to produce a new list of grid points that makes up the solvent accessible areas. For the sets of grid points, the centre of gravity and volume of the void were calculated. The overall solvent accessible volume was calculated, along with the volume and centre of gravity of individual 'voids'.

Quantum chemical calculations. Density functional theory (DFT) calculations were performed in Gaussian 16[56] using the PBE0 hybrid functional (mixes the Perdew–Burke–Ernzerhof[57] and Hartree–Fock exchange energy in a set 3:1 ratio) with the 6-31 G* basis set for H, B, C, N, O, F, and S atoms[58,59] and LanL2DZ effective core potentials for Ag atoms[60,61]. The single-crystal structure was chosen as the initial guess for ground-state geometry optimization, and all reported stationary points were verified as true minima by the absence of negative eigenvalues in the vibrational frequency analysis. The calculated absorption spectra were obtained from GaussSum 2.1[62]. Hirshfeld population analysis was conducted by Multiwfn 3.4[63]. Considering the ISC occurs at the excited states, the time-dependent DFT calculations were further carried out with the B3LYP/def2-SVP level based on the optimized structures. The spin-orbit coupling (SOC) matrix elements for the four systems were computed using the spin-orbit mean-field (SOMF) approach in the B3LYP/def2-SVP level in the ORCA 4.1.2 package[64]. The resolution of the identity (RI) approximation was used during the SOC calculations with the RIJONX flag to speed up the self-consistent field (SCF) convergence during each step. The auxiliary basis sets used with the RI approximation are built automatically by ORCA[65,66]. Over 3000 basis functions were included to create the molecular orbitals, and a typical calculation of 20 singlet and 20 triplet roots were calculated considering the molecules are extremely large (>300 atoms for each).

Luminescence measurements. All solid-state $Ag_{12}bpy-NH_2$, $Ag_{12}bpy-CH_3$, and $Ag_{12}bpy-NH_2/CH_3$ (1:100) samples were evacuated before the collection of luminescence spectra, in addition to solvent-dependent luminescence measurements in Supplementary Fig. 12. Steady-state photoluminescence (PL) spectroscopy, three-dimensional excitation-emission matrix (3D-EEM) luminescence spectroscopy, and emission decay spectroscopy were performed on a HORIBA instrument.

Oxygen-sensing measurements. The $Ag_{12}bpy-NH_2$ samples were placed in a holder in a gas absorption analyser (BEL-max physisorption analyser, Micro-tracBEL Belsorp Max with an ultimate vacuum of 6.7×10^{-7} Pa) to precisely control the O_2 pressure at nearly anaerobic conditions, and this apparatus was connected to a spectrofluorometer (HORIBA FluoroLog-3) by an optical fibre to obtain a luminescence signal readout (see Supplementary Fig. 13). For the range from 20 ppm to air, standard mixed gases of O_2 and N_2 from Henan Yuanzheng Special Gas Development Co., Ltd., were used.

Data availability

Data supporting the findings of this manuscript are available from the corresponding authors upon reasonable request. The X-ray crystallographic coordinates for structures reported in this article have been deposited at the Cambridge Crystallographic Data Centre (CCDC) under deposition number CCDC: 1963529 ($Ag_{12}bpy-NH_2$), 1963530 ($Ag_{12}bpy-CH_3$), 1963528 ($Ag_{12}bpy-CH_3 \cdot O_2$).

References

1. Nakano, T., Hoshi, K. & Baba, S. Effect of background gas environment on oxygen incorporation in TiN films deposited using UHV reactive magnetron sputtering. *Vacuum* **83**, 467–469 (2008).
2. Wang, X.-D. & Wolfbeis, O. S. Optical methods for sensing and imaging oxygen: materials, spectroscopies and applications. *Chem. Soc. Rev.* **43**, 3666–3761 (2014).
3. Wang, X.-D. & Wolfbeis, O. S. Fiber-optic chemical sensors and biosensors (2008–2012). *Anal. Chem.* **85**, 487–508 (2013).
4. Zhou, Y. et al. Long-lived room-temperature phosphorescence for visual and quantitative detection of oxygen. *Angew. Chem. Int. Ed.* **58**, 12102–12106 (2019).
5. Lehner, P., Staudinger, C., Borisov, S. M. & Klimant, I. Ultra-sensitive optical oxygen sensors for characterization of nearly anoxic systems. *Nat. Commun.* **5**, 4460 (2014).
6. Lu, X. & Winnik, M. A. Luminescence quenching in polymer/filler nanocomposite films used in oxygen sensors. *Chem. Mater.* **13**, 3449–3463 (2001).
7. Feng, Y., Cheng, J., Zhou, L., Zhou, X. & Xiang, H. Ratiometric optical oxygen sensing: a review in respect of material design. *Analyst* **137**, 4885–4901 (2012).
8. Liu, S.-Y. et al. Porous Cu(I) triazolate framework and derived hybrid membrane with exceptionally high sensing efficiency for gaseous oxygen. *Adv. Funct. Mater.* **24**, 5866–5872 (2014).
9. Xu, R. et al. Nanoscale metal–organic frameworks for ratiometric oxygen sensing in live cells. *J. Am. Chem. Soc.* **138**, 2158–2161 (2016).
10. Lan, G. et al. Multifunctional nanoscale metal–organic layers for ratiometric pH and oxygen sensing. *J. Am. Chem. Soc.* **141**, 18964–18969 (2019).
11. Wu, S., Min, H., Shi, W. & Cheng, P. Multicenter metal–organic framework-based ratiometric fluorescent sensors. *Adv. Mater.* **32**, 1805871 (2019).
12. Zhang, K.-Y. et al. Dual-phosphorescent iridium(III) complexes extending oxygen sensing from hypoxia to hyperoxia. *J. Am. Chem. Soc.* **140**, 7827–7834 (2018).
13. Zhao, J., Wu, W., Sun, J. & Guo, S. Triplet photosensitizers: from molecular design to applications. *Chem. Soc. Rev.* **42**, 5323–5351 (2013).
14. Demchenko, A. P., Tomin, V. I. & Chou, P.-T. Breaking the Kasha rule for more efficient photochemistry. *Chem. Rev.* **117**, 13353–13381 (2017).
15. McClenaghan, N. D., Leydet, Y., Maubert, B., Indelli, M. T. & Campagna, S. Excited-state equilibration: a process leading to long-lived metal-to-ligand charge transfer luminescence in supramolecular systems. *Coord. Chem. Rev.* **249**, 1336–1350 (2005).
16. Yaghi, O. M., Kalmutzki, M. J. & Diercks, C. S. *Introduction to Reticular Chemistry: Metal-organic frameworks and covalent organic frameworks.* https://doi.org/10.1002/9783527821099 (2019).
17. Pei, X., Bürgi, H.-B., Kapustin, E. A., Liu, Y. & Yaghi, O. M. Coordinative alignment in the pores of MOFs for the structural determination of N-, S-, and P-containing organic compounds including complex chiral molecules. *J. Am. Chem. Soc.* **141**, 18862–18869 (2019).
18. Xu, W. et al. A metal–organic framework of organic vertices and polyoxometalate linkers as a solid-state electrolyte. *J. Am. Chem. Soc.* **141**, 17522–17526 (2019).
19. Karmakar, A., Samanta, P., Desai, A. V. & Ghosh, S. K. Guest-responsive metal–organic frameworks as scaffolds for separation and sensing applications. *Acc. Chem. Res.* **50**, 2457–2469 (2017).
20. Lustig, W. P. et al. Metal–organic frameworks: functional luminescent and photonic materials for sensing applications. *Chem. Soc. Rev.* **46**, 3242–3285 (2017).
21. Lan, G. et al. Multifunctional nanoscale metal–organic layers for ratiometric pH and oxygen sensing. *J. Am. Chem. Soc.* **141**, 18964–18969 (2019).
22. An, J., Shade, C. M., Chengelis-Czegan, D. A., Petoud, S. & Rosi, N. L. Zinc-adeninate metal-organic framework for aqueous encapsulation and sensitization of near-infrared and visible emitting lanthanide cations. *J. Am. Chem. Soc.* **133**, 1220–1223 (2011).
23. Luo, T.-Y. et al. Luminescence "Turn-On" detection of gossypol using Ln^{3+}-based metal–organic frameworks and Ln^{3+} salts. *J. Am. Chem. Soc.* **142**, 2897–2904 (2020).
24. Dou, Z. et al. Luminescent metal–organic framework films as highly sensitive and fast-response oxygen sensors. *J. Am. Chem. Soc.* **136**, 5527–5530 (2014).
25. Cui, Y., Yue, Y., Qian, G. & Chen, B. Luminescent functional metal–organic frameworks. *Chem. Rev.* **112**, 1126–1162 (2012).
26. Furukawa, H., Cordova, K. E., O'Keeffe, M. & Yaghi, O. M. The chemistry and applications of metal-organic frameworks. *Science* **341**, 1230444 (2013).
27. Zhang, Y.-M. et al. Luminescent sensors based on metal-organic frameworks. *Coord. Chem. Rev.* **354**, 28–45 (2018).
28. Hu, Z.-C., Benjamin, J. D. & Li, J. Luminescent metal–organic frameworks for chemical sensing and explosive detection. *Chem. Soc. Rev.* **43**, 5815–5840 (2014).
29. Shimomura, S. et al. Selective sorption of oxygen and nitric oxide by an electron-donating flexible porous coordination polymer. *Nat. Chem.* **2**, 633–637 (2010).
30. Rieth, A. J., Wright, A. M. & Dincă, M. Kinetic stability of metal–organic frameworks for corrosive and coordinating gas capture. *Nat. Rev. Mater.* **4**, 708–725 (2019).
31. Culp, J. T., Madden, C., Kauffman, K., Shi, F. & Matranga, C. Screening Hofmann compounds as CO_2 sorbents: nontraditional synthetic route to over 40 different pore-functionalized and flexible pillared cyanonickelates. *Inorg. Chem.* **52**, 4205–4216 (2013).
32. Li, J.-R., Kuppler, R. J. & Zhou, H.-C. Selective gas adsorption and separation in metal–organic frameworks. *Chem. Soc. Rev.* **38**, 1477–1504 (2009).
33. Huang, R.-W. et al. Hypersensitive dual-function luminescence switching of a silver-chalcogenolate cluster-based metal–organic framework. *Nat. Chem.* **9**, 689–697 (2017).
34. Alhilaly, M. J. et al. Assembly of atomically precise silver nanoclusters into nanocluster-based frameworks. *J. Am. Chem. Soc.* **141**, 9585–9592 (2019).

35. Wang, Z.-Y. et al. Atomically precise site-specific tailoring and directional assembly of superatomic silver nanoclusters. *J. Am. Chem. Soc.* **140**, 1069–1076 (2018).

36. Huang, R.-W. et al. Tandem silver cluster isomerism and mixed linkers to modulate the photoluminescence of cluster assembled-materials. *Angew. Chem. Int. Ed.* **57**, 8560–8566 (2018).

37. Dong, X.-Y., Huang, H.-L., Wang, J.-Y., Li, H.-Y. & Zang, S.-Q. A flexible fluorescent SCC-MOF for switchable molecule identification and temperature display. *Chem. Mater.* **30**, 2160–2167 (2018).

38. Wang, J.-Y. et al. A hydrophobic semiconducting metal–organic framework assembled from silver chalcogenide wires. *Chem. Commun.* **56**, 2091–2094 (2020).

39. Jin, R., Pei, Y. & Tsukuda, T. Controlling nanoparticles with atomic precision. *Acc. Chem. Res.* **52**, 1 (2019).

40. Chakraborty, I. & Pradeep, T. Atomically precise clusters of noble metals: emerging link between atoms and nanoparticles. *Chem. Rev.* **117**, 8208–8271 (2017).

41. Jin, R.-C., Zeng, C.-J., Zhou, M. & Chen, Y.-X. Atomically precise colloidal metal nanoclusters and nanoparticles: fundamentals and opportunities. *Chem. Rev.* **116**, 10346–10413 (2016).

42. Kang, X. & Zhu, M. Tailoring the photoluminescence of atomically precise nanoclusters. *Chem. Soc. Rev.* **48**, 2422–2457 (2019).

43. Han, Z. et al. Ultrastable atomically-precise chiral silver clusters with over 95% quantum efficiency. *Sci. Adv.* **6**, eaay0107 (2020).

44. Cummings, S. D. & Eisenberg, R. Tuning the excited-state properties of Platinum (II) diimine dithiolate complexes. *J. Am. Chem. Soc.* **118**, 1949–1960 (1996).

45. You, Y. & Nam, W. Photofunctional triplet excited states of cyclometalated Ir (III) complexes: beyond electroluminescence. *Chem. Soc. Rev.* **41**, 7061–7084 (2012).

46. Xu, S., Chen, R., Zheng, C. & Huang, W. Excited state modulation for organic afterglow: materials and applications. *Adv. Mater.* **28**, 9920–9940 (2016).

47. Tao, Y. et al. Resonance-activated spin-flipping for efficient organic ultralong room-temperature phosphorescence. *Adv. Mater.* **30**, 1803856 (2018).

48. Lower, S. K. & El-Sayed, M. A. The triplet state and molecular electronic processes in organic molecules. *Chem. Rev.* **66**, 199–241 (1966).

49. An, Z. et al. Stabilizing triplet excited states for ultralong organic phosphorescence. *Nat. Mater.* **14**, 685–690 (2015).

50. Zhao, W. et al. Rational molecular design for achieving persistent and efficient pure organic room-temperature phosphorescence. *Chem* **1**, 592–602 (2016).

51. CrysAlis^Pro, Version 1.171.36.31. Agilent Technologies Inc., Santa Clara, CA, USA (2012).

52. O. D. Rigaku, CrysAlisPro Software System, Version 1.171.38.41k, Rigaku Coorporation, Oxford, UK (2015).

53. Sheldrick, G. M. A short history of *SHELX*. *Acta Cryst. A* **64**, 112–122 (2008).

54. Dolomanov, O. V., Bourhis, L. J., Gildea, R. J., Howard, J. A. K. & Puschmann, H. *OLEX2*: a complete structure solution, refinement and analysis program. *J. Appl. Cryst.* **42**, 339–341 (2009).

55. Sheldrick, G. M. Crystal structure refinement with *SHELXL*. *Acta Cryst. C.* **71**, 3–8 (2015).

56. Frisch, M. J. et al. Gaussian, Inc. (Wallingford CT, 2016).

57. Adamo., C. & Barone, V. Toward reliable density functional methods without adjustable parameters: the PBE0 model. *J. Chem. Phys.* **110**, 6158–6169 (1999).

58. Hariharan, P. C. & Pople, J. A. The influence of polarization functions on molecular orbital hydrogenation energies. *Theor. Chim. Acta* **28**, 213–222 (1973).

59. Francl, M. M. et al. Self-consistent molecular orbital methods. XXIII. A polarization-type basis set for second-row elements. *J. Chem. Phys.* **77**, 3654–3665 (1982).

60. Hay, P. J. & Wadt, W. R. Ab initio effective core potentials for molecular calculations. Potentials for the transition metal atoms Sc to Hg. *J. Chem. Phys.* **82**, 270–283 (1985).

61. Hay, P. J. & Wadt, W. R. Ab initio effective core potentials for molecular calculations. Potentials for main group elements Na to Bi. *J. Chem. Phys.* **82**, 284–298 (1985).

62. Weigend, F. & Ahlrichs, R. Balanced basis sets of split valence, triple zeta valence and quadruple zeta valence quality for H to Rn: Design and assessment of accuracy. *Phys. Chem. Chem. Phys.* **7**, 3297–3305 (2005).

63. Lu, T. & Chen, F. W. Multiwfn: a multifunctional wavefunction analyzer. *J. Comput. Chem.* **33**, 580–592 (2012).

64. Neese, F. Software update: the ORCA program system, version 4.0. *WIREs Comput. Mol. Sci.* **8**, e1327 (2018).

65. Kendall, R. A. & Früchtl, H. A. The impact of the resolution of the identity approximate integral method on modern ab initio algorithm development. *Theor. Chem. Acc.* **97**, 158–163 (1997).

66. Neese, F. An improvement of the resolution of the identity approximation for the formation of the Coulomb matrix. *J. Comput. Chem.* **24**, 1740–1747 (2003).

Author contributions
S.Q.Z. conceived and designed the experiments. X.Y.D., J.S.Y., and Z.H. conducted the synthesis and characterization. Y.S. and P.L. performed the calculations. C.Z. drew pictures in the manuscript. S.Q.Z., X.Y.D., and Z.Y.W. analyzed the experimental results. X.Y.D., S.Q.Z., and T.C.W.M co-wrote the manuscript.

Competing interests
The authors declare no competing interests.

Additional information
Supplementary information is available for this paper at https://doi.org/10.1038/s41467-020-17200-w.

Correspondence and requests for materials should be addressed to S.-Q.Z.

Peer review information *Nature Communications* thanks Mei Pan and other, anonymous, reviewer(s) for their contributions to the peer review of this work. Peer review reports are available.

Reprints and permission information is available at http://www.nature.com/reprints

Publisher's note Springer Nature remains neutral with regard to jurisdictional claims in published maps and institutional affiliations.